Influence of V-Pits on the Turn-On Voltage of GaN-Based High Periodicity Multiple Quantum Well Solar Cells

Marco Nicoletto, Alessandro Caria, Fabiana Rampazzo, Carlo De Santi, *Member, IEEE*, Matteo Buffolo, Giovanna Mura, Francesca Rossi, Xuanqui Huang, Houqiang Fu, Hong Chen, Yuji Zhao, Gaudenzio Meneghesso, *Fellow, IEEE*, Enrico Zanoni, *Fellow, IEEE*, and Matteo Meneghini, *Senior Member, IEEE*

***Abstract*—Based on combined electrical analysis, microscopy investigation, and two-dimensional simulations we investigate the influence of V-pits on the turn-ON voltage and current-voltage characteristics of high periodicity InGaN-GaN multiple quantum wells solar cells. Experimental measurements indicate that the sample with the thinnest p-GaN layer presents an early turn-ON, which is not present for thicker p-GaN layers. Through technology computer aided design (TCAD) simulations, we show that the early turn-ON is due to the insufficient V-pit planarization, as demonstrated by scanning electron microscopy and transmission electron microscopy analysis. V-pits penetrate the junctions, and locally put the quantum well region in closer connection with the p-side contact. The results provide insight on the role of V-pits on the electrical performance of high-periodicity quantum well devices, and demonstrate the existence of a trade-OFF between the need of a thin p-GaN (to limit short-wavelength absorption) and a thicker p-GaN, to favor V-pit planarization.**

***Index Terms*—Experimental, GaN, InGaN, modeling, multiple-quantum-well, solar cells, V-pits.**

Manuscript received 27 June 2023; revised 26 July 2023; accepted 31 August 2023. Date of publication 15 September 2023; date of current version 7 November 2023. This work was supported in part by European Union – Next Generation EU, within the PNRR project "NEST – Network 4 Energy Sustainable Transition" for the activity at the University of Padova, in part by the National Recovery and Resilience Plan, Mission 4 Component 2 Investment 1.3 - Call for tender 1561 of 11.10.2022 of Ministero dell'Università e della Ricerca, and in part by Arizona State University and Rice University was partially supported by ULTRA, an Energy Frontier Research Center funded by the U.S. Department of Energy, Office of Science, Basic Energy Sciences under Grant# DE-SC0021230. *(Corresponding author: Marco Nicoletto.)*

Marco Nicoletto, Alessandro Caria, Fabiana Rampazzo, Carlo De Santi, Matteo Buffolo, Gaudenzio Meneghesso, and Enrico Zanoni are with the Department of Information Engineering, University of Padova, 35131 Padova, Italy (e-mail: marco.nicoletto.2@studenti.unipd.it; alessandro.caria@unipd.it; fabiana.rampazzo@unipd.it; carlo.desanti@unipd.it; matteo.buffolo.1@unipd.it; gauss@dei.unipd.it; zanoni@dei.unipd.it).

Giovanna Mura is with the University of Cagliari, 09124 Cagliari, Italy (e-mail: giovanna.mura@unica.it).

Francesca Rossi is with the CNR IMEM, 43124 Parma, Italy (e-mail: francesca.rossi@imem.cnr.it).

Xuanqui Huang, Houqiang Fu, and Hong Chen are with the School of Electrical, Computer, and Energy Engineering, Arizona State University, Tempe, AZ 85287 USA (e-mail: xuanqi.huang@asu.edu; houqiang@asu.edu; hong.chen@mpi-halle.mpg.de).

Yuji Zhao is with the School of Electrical, Computer, and Energy Engineering, Arizona State University, Tempe, AZ 85287 USA, and also with the Department of Electrical and Computer Engineering, Rice University, Houston, TX 77005 USA (e-mail: yuji.zhao@rice.edu).

Matteo Meneghini is with the Department of Information Engineering, University of Padova, 35131 Padova, Italy, and also with the Department of Physics and Astronomy, University of Padova, 35122 Padova, Italy (e-mail: matteo.meneghini@unipd.it).

Color versions of one or more figures in this article are available at https://doi.org/10.1109/JPHOTOV.2023.3311891.

Digital Object Identifier 10.1109/JPHOTOV.2023.3311891

I. Introduction

GAN-BASED high periodicity InGaN-GaN multiple quantum wells (MQW) solar cells were proposed as additional components of multijunction solar cells and in concentrator solar harvesting systems [1], [2], to increase the efficiency and use of renewable energy sources countering climate issues. Recently, these devices have also been studied for emerging applications such as wireless power transfer systems [3] and space operations [4], thanks to their reliability and efficiency in harsh environments [5]. During the growth of GaN-based devices on sapphire substrates, the large lattice mismatch and the difference in thermal expansion coefficient between GaN and sapphire leads to the formation of several defects such as stacking faults, inversion domain boundaries and threading dislocations (TD) [6], [7]. These defects can deteriorate the electrical and optical properties of GaN-based devices: in particular, based on transmission electron microscopy (TEM) and atomic force microscopy, different papers reported that TDs disrupt the active region composed by MQWs, leading to the formation of V-defects (or V-pits) [8], [9], [10], [11], [12]. These V-defects have an open hexagonal, inverted pyramid with {10-11} side walls [11]. Several research groups have reported that the causes of V-pits formation are: 1) the increased strain energy in the growth of GaN from the sapphire substrate; 2) the reduced Ga incorporation on the pyramid plane in comparison with (0001) surface planes [11], [12]; 3) the increase in strain energy with increasing layer thickness and indium mole fraction in InGaN quantum wells (QWs) [9], [12]; 4) the relative low temperature used to grow InGaN QWs, which leads to a degraded composition of GaN, since gallium presents limited surface diffusion at these low temperature [13]. V defects are detrimental for the active region of the devices, since they interrupt the periodic structure of the MQWs, creating regions with different well and barrier thickness and also different indium incorporation

and concentration [14], [15], [16], and therefore, a different barrier height in the pyramid plane of the V-pits with respect to (0001) surface plane [10], [17], [18], [19]. Recent studies on the origin of these defects in GaN-based similar devices such as light emitting diodes allowed to understand and control the formation of V-pits: by monitoring the growth temperature, the dimension and the periods of superlattices layers (SL), it is possible to control the density, the physical size and the potential barrier height of the resulting V-pits, thus suppressing the lateral diffusion of carriers towards nonradiative recombination centers related to TDs [20], [21], [22], [23] [9], [13], [24], [25]. In the literature, a detailed analysis of the role of V-pits on the electrical characteristics of high periodicity MQW devices has not been presented so far. The aim of this work is to fill this gap, by improving the understanding on the role of V-pits in III-N devices. First, by focusing on the V-defects analysis, through scanning electron microscopy (SEM) and TEM measurements, the density and dimensions of V-pits is evaluated. Second, through technology computer aided design (TCAD) Synopsys Sentaurus simulations, the main I-V characteristics are reproduced considering V-defects. The results indicate that V-pits play a dominant role in current conduction, especially for the devices with the thinnest p-GaN layer, that lack significant planarization. For such devices, the p-side contact is closer to the MQW, resulting in the formation of localized short circuit paths. A Gaussian distribution of V-pits dimensions and depth is considered, in order to reach a good matching of experimental data. The outcome of this work will be useful for the design of future GaN-based devices with high-periodicity MQWs, ensuring the desired turn-ON voltage and their reliability in harsh environment applications.

II. Experimental Details

The GaN-based solar cells with high-periodicity InGaN/GaN multiquantum wells considered in this article were grown on c-plane (0001) sapphire by metal organic chemical vapour deposition (MOCVD). Fig. 1 presents the device under test, which consist of 2 μm n-GaN (Si doped, Si concentration [Si] $= 3 \times 10^{18}$ cm^{-3}) layer over the sapphire substrate and a 125 nm n$^+$-GaN (Si doped, Si concentration [Si] $= 2 \times 10^{19}$ cm^{-3}) layer, to create an ohmic contact. Above the n$^+$-GaN layer, the active region is composed by a periodic structure of 30 pairs of undoped $In_{0.15}Ga_{0.85}N$ quantum wells (3 nm, with an indium mole fraction of 15%) and GaN barriers (7 nm). Above the active region, a 5 nm p-$Al_{0.15}Ga_{0.85}N$ electron blocking layer (EBL) (Mg doped, 2×10^{19} cm^{-3}) is inserted, to enhance carrier collection at the p-side of the devices by reducing the recombination rate and increasing the carrier lifetime. Above the EBL, a p-GaN layer (Mg doped, concentration [Mg] $= 2 \times 10^{19}$ cm^{-3}) with different thickness is grown: 50 nm (Sample 2 A), 100 nm (Sample 1 A), and 150 nm (Sample 2B). Finally, a 10 nm p$^+$-GaN contact layer to create an ohmic contact (Mg doped, concentration [Mg] $> 2 \times 10^{19}$ cm^{-3}) is formed under a semitransparent 130 nm indium-tin oxide (ITO) layer, which is deposited by dc-sputtering on top of the mesa as a current spreading layer with postannealing in N_2/O_2 at 500 °C. Devices were then processed by standard lithography into 1 mm $\times$ 1 mm solar cells and finally, Ti/Al/Ni/Au

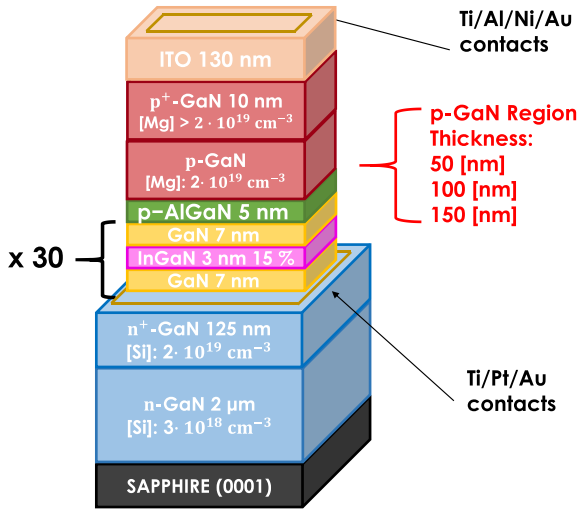

Fig. 1. Structure of the devices under test. Devices with different thickness of the p-GaN layer (50, 100, and 150 nm) were considered.

ring contacts and Ti/Pt/Au grid contacts were deposited via electron beam evaporation around the perimeter and on the top of the mesa, respectively, to form cathode and anode. Other details of the device could be found in [26]. Device characterization was performed on-wafer on a thermal-controlled baseplate heated by a ceramic heater at 35 °C ambient temperature. A semiconductor parameter analyzer was used to provide bias to the device and to obtain high accuracy electrical measurements. Details about the setup can be found elsewhere [27]. SEM characterization to obtain filtering grid in-beam backscattered electrons (f-BSE) images were performed through the TESCAN SOLARIS microscope, which is a dual beam system containing the TriglavTM immersion optics column and the OrangeTM Ga ion optics column attached to one chamber, which combines the imaging qualities of a SEM with the possibility of surface modification using a focused ion beam (FIB). Exploiting FIB characterization, a lamella of the analyzed device was obtained, to characterize the cross-sectional structure of the sample. The cross-sectional structure was analyzed by a TEM using a JEOL JEM-2200FS field emission microscope equipped with an in-column Ω filter, operated at 200 keV. Imaging was carried out in scanning transmission electron microscope (STEM) mode using a high-angle annular dark-field detector that exploits atomic-number (Z) contrast.

III. Device Characterization

An in-depth analysis of the role of the thickness of the p-GaN layer in the degradation of these GaN-based devices when submitted to constant optical power stress is presented in [28] and [29]; through an indirect analysis, this article found that a thicker p-GaN layer reduces the amount of defects reaching the active region in a thermally-activated diffusion process. However, an analysis of the influence of the p-GaN layer thickness in the current-voltage characteristic was not presented to date. Fig. 2 reports the nonilluminated current-voltage characteristics of the three samples with different p-GaN layer thickness. The sample with the thinnest p-GaN layer (50 nm, blue curve in

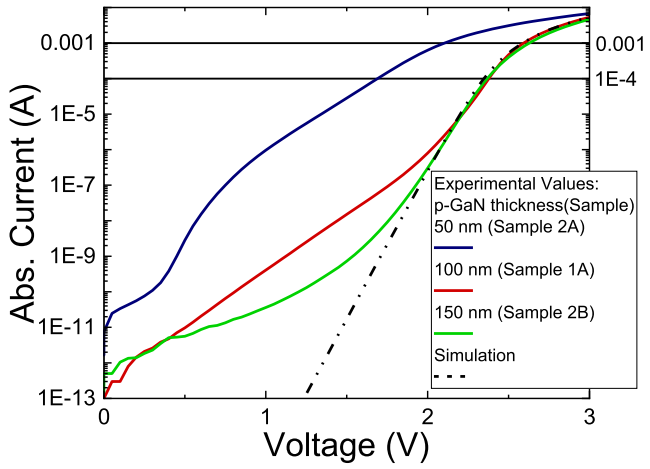

Fig. 2. Nonilluminated current-voltage characteristics of the three samples with different p-GaN layer thickness (continuous colored lines, see legend). There is an evidence of an early turn ON in the sample having the thinnest p-GaN layer. Device simulation without V-pits implementation (Black dotted curve, which is representative for simulation with 50, 100, and 150 nm p-GaN thickness.): no differences between p-GaN thickness in device turn-ON voltage and current-voltage characteristic is present without V-defects implementation.

TABLE I
TURN-ON VOLTAGE OF SAMPLE WITH DIFFERENT P-GAN THICKNESS

p-GaN thickness	50 nm	100 nm	150 nm
Current [mA]	Turn-on Voltage [V]:	Turn-on Voltage [V]:	Turn-on Voltage [V]:
1	2.1	2.6	2.65
0.1	1.7	2.35	2.35

Fig. 2) presents an early turn-ON with respect to the thicker ones (100 nm and 150 nm, respectively, red and green curve in Fig. 2). Curves in Fig. 2 are representative of several solar cells of each sample with different p-GaN thickness. Considering as the turn-ON voltage of the main diode the voltage at which a current of 1 mA or 0.1 mA is reached (black continuous curves in Fig. 2, the turn-ON values presented in Table I were measured.

Furthermore, the shape of the current-voltage characteristic below the main diode turn-ON differs between samples with different p-GaN thickness. Typically, current flow at low voltages is influenced by traps located in the active region, through trap-assisted tunneling [30], [31], [32], and other trap-mediated conduction processes [33]. Thus, the higher current at low bias level in sample with the thinnest p-GaN layer qualitatively indicates a lower quality of the analyzed device with respect to the others [26]. The three samples were grown on c-plane (0001) sapphire by MOCVD under similar growth conditions, i.e., they have a same thickness of the n-GaN region, and identical well and barrier thickness (i.e., same ratio, R) and indium composition (15%). The increased strain energy in the growth of GaN from the sapphire substrate and a relatively high indium composition (>10%) will increase the strain at the InGaN/GaN interface leading to the origination of pits in correspondence of dislocations [25]: as described in prior reports [11], a fast vertical growth rate of (0001) facet with respect to the slow lateral growth rate of the inclined facets {10-11} [36] would lead to the origination of the V defects. Since the density and dimension of the originated V-defects is known to be influenced by the indium composition in the MQWs, by the thickness of GaN barrier and InGaN well, and by the number of MQWs [34], [35], we expect similar densities and sizes of V-pits observable on the surface of the devices due to their similar growth conditions [37] and structure, as we can observe by SEM imaging. Fig. 3 reports the In-Beam f-BSE images obtained by the TESCAN SOLARIS microscope. To evaluate the density of V-defects, five In-beam f-BSE images with an area of $20\times15\ \mu m^2$ were taken on each sample. Considering that black dots correspond to V-pits, a density of 8.6×10^7, 7.9×10^7, and $1\times10^8\ cm^{-2}$ was calculated for samples with p-GaN thickness of 150, 100, and 50 nm, respectively [see Fig. 3(a)–(c)]. Finally, five In-Beam f-BSE high magnification images were acquired over an area of $2\times1.5\ \mu m^2$, which allowed to evaluate the shape and size of the V-depression with higher resolution: the well-known hexagonal shape of the V-pits is recognized, with diagonal lengths in a range of 160 and 100 nm for all samples regardless of the size of the p-GaN [see Fig. 3(d)–(f)]. Based on the comparison between these images, we can state that the early turn-ON in the sample with thinner p-GaN layer is not related to different V-pits density, as was expected from literature [34]. Fig. 4 shows the STEM image of the lateral cross section of the device with 100 nm p-GaN; two V-pits with different depths are observed. The situation is also representative for the other samples with different thickness of the p-GaN layer: we observed that the V-depressions originate in the last quantum wells of the device; also, the thickness of the p-GaN layer is smaller above the depression, compared to the lateral regions where the V-pit is not present. The larger the thickness of the p-GaN layer, the greater the planarization of the V-depression, resulting in a greater distance between the active region composed of MQWs and the ITO layer.

IV. SIMULATION PARAMETERS

To investigate the influence of V-pits in device turn-ON, we performed numerical simulations by the TCAD Sentaurus suite from Synopsys Inc [38], [39]. First, the different layers with their respective dimensions were implemented. Regarding intentional doping, magnesium (Mg) traps were placed at the p-side and silicon (Si) traps at the n side with concentrations according to the previous section (see Table II). The ionization energy levels reported also in Table II were chosen in agreement with prior experimental characterization [26]. Second, Shockley–Read–Hall (SRH), radiative and Auger–Meitner generation-recombination mechanisms, thermionic emission, and barrier-tunneling processes were considered with recombination parameters chosen in agreement with the literature, as reported in Table II.

V. PARASITIC RESISTANCES AND CONTACTS

The values of the parasitic resistances of the device were evaluated by experimental characterizations and included in the simulations. Thus, a series resistance (Rs) of 36 Ω, which considers nonideal contacts due to partial activation of doping

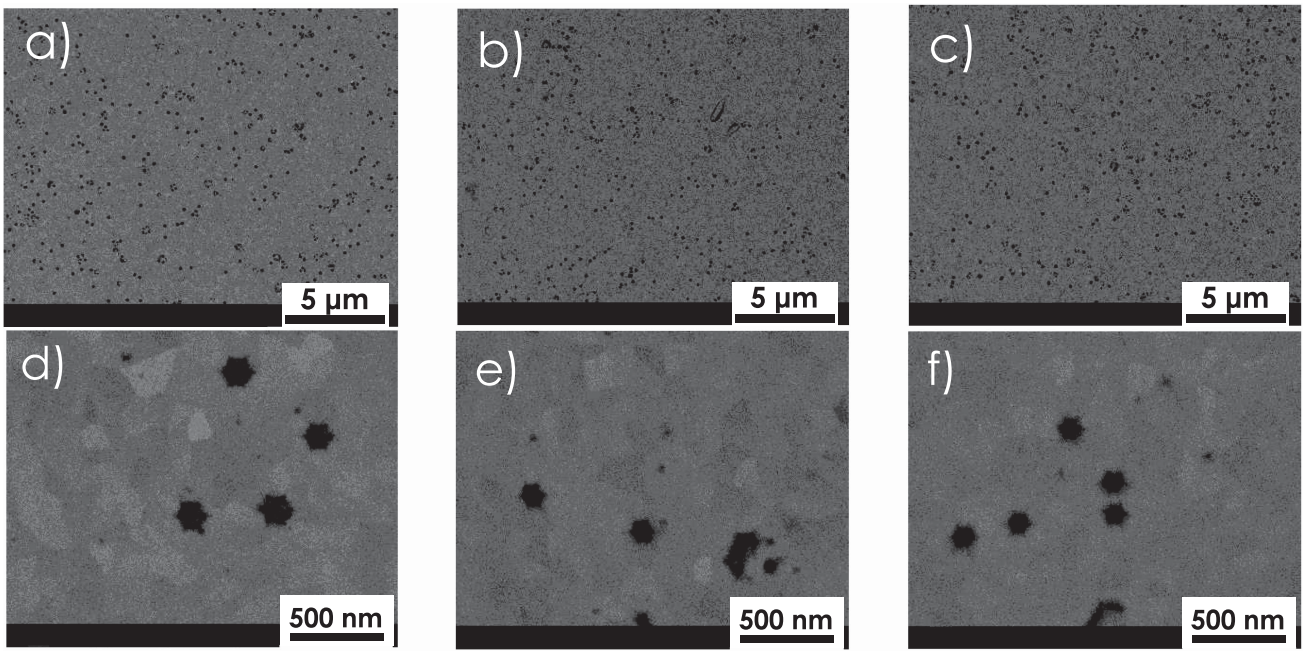

Fig. 3. In-Beam f-BSE. Large area images (20×15 μm^2) to evaluate density. Samples with different p-GaN thickness: (a) 150 nm, (b) 100 nm, and (c) 50 nm. Zoom (2 μm$\times1.5$ μm) to evaluate V-pit dimensions. Samples with different p-GaN thickness: (d) 150 nm, (e) 100 nm, and (f) 50 nm.

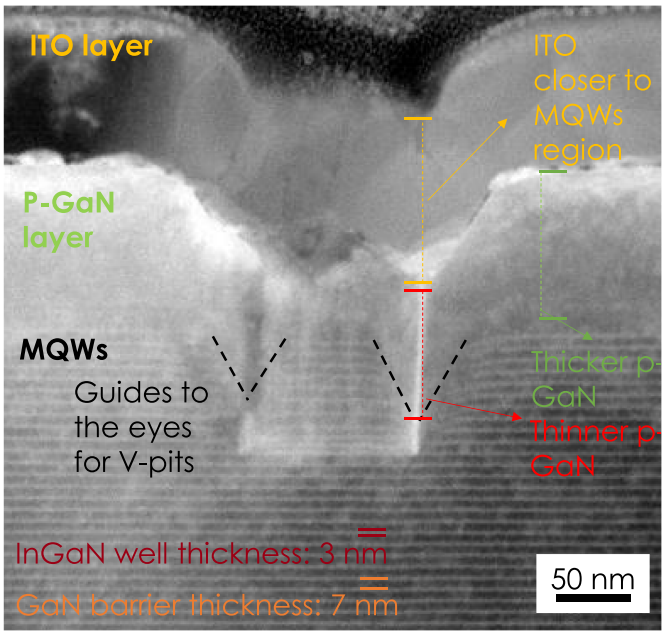

Fig. 4. STEM image of lateral cross-section of sample with 100 nm of p-GaN. The dashed black curves serve as a guide for the eyes. A different thickness of p-GaN is observed above the V-pit compared with the surrounding area, resulting in ITO layer being closer to the active region.

and other nonidealities [44], and a shunt resistance (Rsh) of 5×10^9 Ω, which models the current leakage near 0 V, were added to the device. The n-type contact was considered as an ideal ohmic contact, whereas a Schottky contact was considered on the p-side. The thickness and doping of the thin p^+-GaN layer was set according to device manufacturers information [26]. The work function (WK) of the ITO layer was chosen in the range of WKs known in the literature for the ITO, i.e., $\Phi_{BE} = 4.3$ eV [45], to match the threshold voltage and the overall influence of Rs in the current-voltage characteristic of the device, considering the resistivity ρ due to the Schottky contact and tunneling at p-contact given by [46]

$$\rho = \frac{k}{\pi\, q\, T A^*} \sin\left(\pi d_1 k T\right) \exp\left(\frac{q\Phi_{BE}}{E_{00}}\right). \tag{1}$$

Here, k is the Boltzmann constant, q is the electron charge, T is the absolute temperature, A^* is the Richardson constant ($A^* = 26$ A/K^{2}cm^2), d_1 depends on the position of the Fermi level, E_{00} and Φ_{BE}, where E_{00} is a tunneling parameter. With these parameters, the simulated current-voltage characteristic is presented in Fig. 2: no variation is observed in the simulation by changing p-GaN thickness. The black curve in Fig. 2 is representative for device simulation with 50, 100, and 150 nm: by varying the thickness of the p-GaN layer, the effect of an early turn-ON voltage for the device with the thinnest p-GaN layer is not present. Instead, independently on the p-GaN thickness, the simulated dark current-voltage characteristic match the turn-ON voltage and the series resistance of the samples with thicker p-GaN layer.

VI. V-PIT Implementation

To match the early turn-ON voltage observed in the experimental data, V-pits were then implemented. Fig. 4 reports the STEM image of the cross section of sample with 100 nm p-GaN thickness. It is evident that in the side faces of the V-pit, layers above the MQWs region grow differently than in the planar region where V-pits are not present. This results in a different thickness of the p-GaN and p^+-GaN layers above the MQWs region, and therefore in an ITO layer closer to the MQWs region.

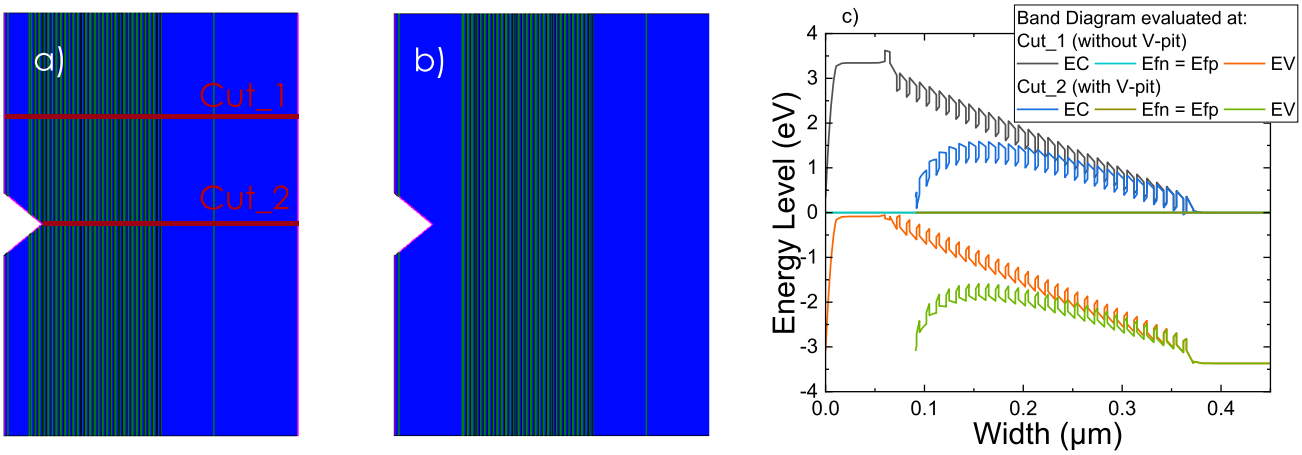

Fig. 5. V-pit gap implementation in simulation of sample with (a) 50 nm and (b) 150 nm p-GaN. (c) Band-diagram along a V-pit (Cut_2) and along a region without V-pit (Cut_1) of sample with 50 nm p-GaN.

TABLE II
DEVICE MOST RELEVANT MATERIAL AND SIMULATION PARAMETERS: RECOMBINATION PARAMETERS AND ACTIVATION ENERGIES WERE CHOSEN IN AGREEMENT WITH PREVIOUS RESULTS [32], [40], [41], [42], [43]. OTHER PARAMETERS WILL BE INTRODUCED IN THE NEXT SECTIONS

	GaN	**AlGaN**	**InGaN**
x content	-	Al: 15 % Ga: 85 %	In: 15 % Ga: 85 %
SRH lifetime (s)	5×10^{-8}	5×10^{-8}	5×10^{-8}
B (cm^3s^{-1})	2×10^{-10}	1.9×10^{-10}	2×10^{-10}
C (cm^6s^{-1})	1×10^{-30}	1×10^{-30}	1×10^{-30}
Donor activation energy [meV]	50	-	-
Acceptor activation energy [meV]	200	200	-
	Device parameters:		
Series resistance R_S (Ω)	36		
Parallel resistance R_P (Ω)	5×10^9		
Piezoelectric Polarization	35 %		
	GaN barrier and InGaN well		
Electron barrier tunneling mass	$m_{t,e} = 0.08$		
Hole barrier tunneling mass	$m_{t,h} = 0.08$		
Defect energy distribution	Uniform distribution centered at the intrinsic Fermi level E_i		
Total energy window	$E_{sigma} = 0.3\ eV$		
Defect concentration	$N_T = 1 \times 10^{16}\ cm^3$		
Capture cross section	$\sigma = 5 \times 10^{-15}\ cm^2$		

In the two-dimensional (2-D) simulation V-pit was implemented as an equilateral triangle gap that extends to the regions below, as shown in Fig. 5. In the edge that contours the V-pit cavity, the p-contact is present, since it is observed that the V-pit cavity is filled by the ITO layer, that enters deeper in the device (see Fig. 4).

The equilateral triangular shape of the gap derives from the known pyramidal shape of the V-pit depression, where an angle of about 60° is observed between opposite pyramid facets [47]. The length of the base of the equilateral triangle gap was set equal to the value found in the SEM characterization (see Fig. 3), and thus, in the range of 100–160 nm. The depth of the V-pit was set in accordance with the size of the base, following the geometry of the equilateral triangle. Finally, the depth distribution was a fitting parameter, defined based on a Gaussian distribution, as will be discussed later. The V-pit density was simulated considering the ratio between the length of the triangle base and the total size of the simulated portion of the cell. In a simulation where the V-pit extends until the region with the multiple quantum wells, Fig. 5(a), the percentage of piezoelectric charge activation in the MQWs adjacent to the V-pit was decreased from the value of 35% (see Table II), used for the entire MQWs region, to a value of 10%, as a result of the different growth rate of p-GaN over the V-pit facets, where less piezoelectric charge activation is observed [48]. The 2-D rather than 3-D simulations were performed, as the width of the triangle obtained by changing the angle of the vertical cross-sectional plane (along 0001) of the hexagonal pyramid was not a factor influencing the conduction mechanisms, unlike the depth of the V-pit, as will become clear later. In Fig. 5(a) and (b), a V-pit equal in size and depth is inserted into the device structure with 50 nm (a) and 150 nm (b) p-GaN thickness: however, for the sample with thicker p-GaN, the MQWs region is farther from the contact placed on the edge of the V-pit, as a consequence of the larger thickness of p-GaN. In fact, a thicker p-GaN layer will increase the planarization of the gap originated by the V-pit, resulting in a higher distance between the p-contact and the MQWs region and approaching the ideal situation of a device with uniform p-GaN layer thickness. Looking at the band diagram in Fig. 5(c), it can be seen that the closer p-contact to the MQWs region [diagram intercepting the V-pit, Cut_2 in Fig. 5(c)] results in a decrease in the potential barrier from the n-side to the p-side, compared with the situation where there is an entire layer of p-GaN, which originate the potential barrier at the p-side [diagram not intercepting the V-pit, Cut_1 in Fig. 5(c)]. The effect of the closer contact is in fact to short-circuit the MQWs active region with

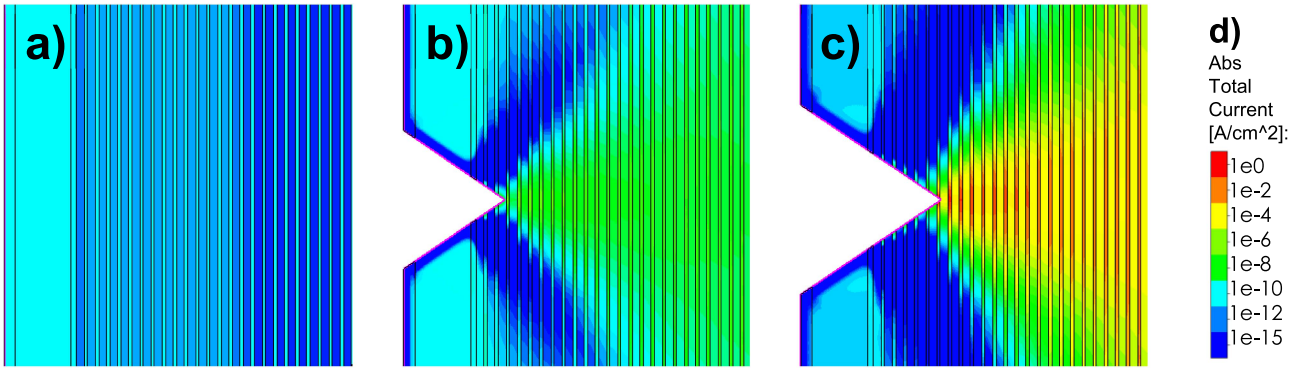

Fig. 6. Increase in absolute total current as function of V-pits depth: (a) no Vpit; (b) V-pit depth: 90 nm (c) V-pit depth: 120 nm; (d) total abs current of previous simulations.

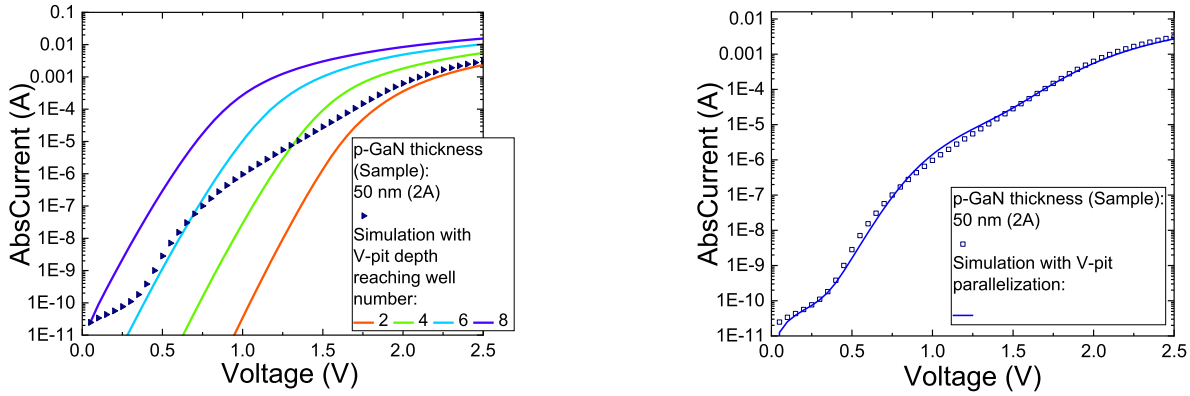

Fig. 7. Current–Voltage characteristic of simulation with increasing V-pit depth in device with 50 nm p-GaN (a); simulation matching the turn-ON and current-voltage characteristic of sample with 50 nm p-GaN (b).

the p contact, eliminating the potential barrier, originated by the p-GaN layer, in correspondence of the V-pit, approaching the situation where the p-GaN layer is not present.

The deeper the V-pit, the lower the distance between the MQWs active region; this results in a higher current due to an enhanced lowering in the potential barrier. Fig. 6 reports a qualitative graph of the absolute value of the total current in the device with 50 nm p-GaN thickness, without V-pit implementation (a), and with V-pit of different depths and dimensions (b) and (c), at 1.5 V. Considering the color map representative of the total current [see Fig. 6(d)], a higher amount of current is observed in the device with the deepest V-pit. As observable in Fig. 6(a)–(c), the overall effect is not uniform over the entire device structure, but is evident in correspondence of the V-pit, and increases as the depth of V-pits increases. Fig. 7(a) shows the current-voltage characteristic of the device with 50 nm of p-GaN with V-pits of increasing depths: from 85 nm (with a base of 100 nm, i.e., a V-shaped depression filled with ITO reaching the second well/barrier interface starting from the p-side, red solid curve), to 145 nm (with a base of 165 nm, i.e., a V-shaped depression filled with ITO reaching the eighth well/barrier interface starting from the p-side, blue solid curve). As the depth of the V-pit increases, the turn-ON voltage decreases and the current increases. The contribution of the different depths was tuned to fit the experimental value of the current-voltage characteristics, since even from SEM images, no particular trend regarding the size of V-pits was observable, other than a higher occurrence of smaller diameter V-pits. In particular, the current-voltage characteristic of the device with only shallower V-pits matches the experimental turn-ON voltage, which occurs earlier than in the samples with thicker p-GaN.

TABLE III
GAUSSIAN DISTRIBUTION OF DIFFERENT DEPTHS V-PITS

V-pit depth [nm]:	85	105	125	145
Distribution	90 %	9 %	0.57 %	0.43 %

This can be explained as an effect of a p-side contact closer to the active region. The other simulated I-V curves, with deeper V-pits, present a very low turn-ON. Given the large variability in the size of the V-pits, we decided to consider a Gaussian depth distribution, rather than a single value, since it is more representative of a realistic case [49], [50]. In this way, the device I-V characteristics were reproduced even at low bias voltages. By using the parameters in Table III, we could match the entire current voltage characteristic of the device, as shown in Fig. 7(b).

Similar simulations, with V-pits of identical size, depth, and concentrations, were also performed for the other two samples

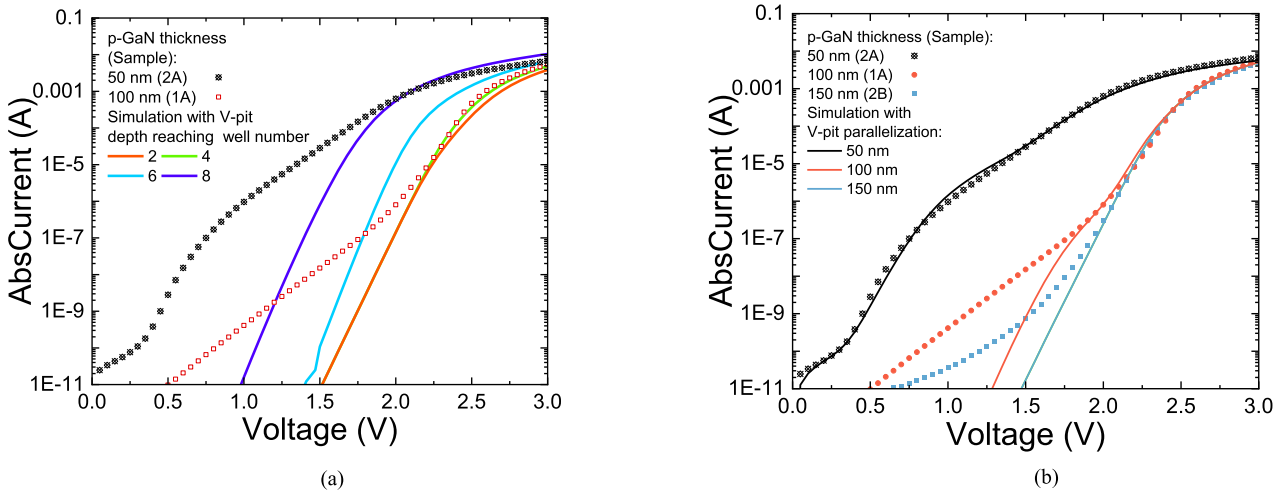

Fig. 8. Current–Voltage characteristics with increasing V-pit depth in a device with 100 nm p-GaN (a); simulation matching only the turn-ON, but not the current–voltage characteristic below main diode turn-ON, for sample with 100 nm p-GaN (red curve) and 150 nm p-GaN (blue curve) (b).

by simply increasing the thickness of the p-GaN region. In this way, the p-contact contouring the V-pit resulted to be farther from the MQWs region, leading to a smaller decrease in the turn-ON voltage compared to the sample with 50 nm p-GaN, as can be seen by the I-V curves in Fig. 8(a). The situation is also representative for the sample with 150 nm, where a greater distance between the MQWs region and the V-pit contact results in a lower decrease of the turn-ON voltage, as the depth of the V-pits increases. Finally, by considering the same Gaussian distribution of the depth of the various V-pits as before, for samples with thicker p-GaN thickness it is possible to match only the turn-ON voltage of the device, but not the entire current voltage characteristic [see Fig. 8(b)]. Therefore, for these samples, for which V-pits are expected to have a smaller influence on the characteristics, the current flow below the main diode turn-ON is more affected by other conduction processes, possibly trap-assisted tunneling phenomena [30], [31], [32], and other trap-mediated conduction processes [33]. In conclusion, incomplete V-pit planarization, in the case of thinnest p-GaN layer, leads to lower overall sample quality, causing poor electrical performance of the devices, especially at low/moderate current levels [28], [29].

VII. Conclusion

In conclusion, we analyzed and modeled the impact of V-pits on the electrical characteristics of GaN-based high periodicity InGaN-GaN MQWs solar cells. First, we demonstrated differences in the nonilluminated current-voltage characteristics of devices with different p-GaN layer thickness: devices with a thinner p-GaN layer showed an early turn-ON voltage. SEM and TEM analysis demonstrated a similar density and size of V-pits for devices with different p-GaN thickness. Then, through TCAD simulations, we showed that the differences in I-V curves, and in particular the early of the turn-ON voltage observed for low p-GaN thickness, can be explained by the penetration of V-pits towards the MQW region. This reduces the distance between the p-side contact and the MQW region of the devices, and leads to a higher local leakage. Through the definition of a Gaussian distribution of depths of V-pits, based on experimental considerations, we were able to reproduce by TCAD the behavior of the electrical characteristics. Finally, results reveal the importance of a full surface planarization in high-periodicity devices for light collection: a tradeoff exists between the need for a thin p-GaN (to minimize short-wavelength light absorption), and for a thicker p-GaN, to minimize the impact of V-pits in favoring leakage current conduction.

Acknowledgment

The views and opinions expressed are however only those of the authors and do not necessarily reflect those of the European Union or the European Commission. Neither the European Union nor the European Commission can be held responsible for them

References

[1] C. Jiang et al., "Enhanced photocurrent in InGaN/GaN MQWs solar cells by coupling plasmonic with piezo-phototronic effect," *Nano Energy*, vol. 57, pp. 300–306, 2019, doi: 10.1016/j.nanoen.2018.12.036.

[2] G. Moses et al., "InGaN/GaN multi-quantum-well solar cells under high solar concentration and elevated temperatures for hybrid solar thermal-photovoltaic power plants," *Prog. Photovolt., Res. Appl.*, vol. 28, pp. 1167–1174, Aug. 2020, doi: 10.1002/pip.3326.

[3] C. de Santi et al., "GaN-based laser wireless power transfer system," *Materials*, vol. 11, no. 1, Jan. 2018, Art. no. 153, doi: 10.3390/MA11010153.

[4] Y. Zhao et al., "InGaN-based solar cells for space applications," in *Proc. Midwest Symp. Circuits Syst.*, 2017, pp. 954–957, doi: 10.1109/MWSCAS.2017.8053083.

[5] D.-H. Lien et al., "Harsh photovoltaics using InGaN/GaN multiple quantum well schemes," *Nano Energy*, vol. 11, pp. 104–109, Jan. 2015, doi: 10.1016/j.nanoen.2014.10.013.

[6] X. H. Wu et al., "Defect structure of metal-organic chemical vapor deposition-grown epitaxial (0001) GaN/Al2O3," *J. Appl. Phys.*, vol. 80, no. 6, Jun. 1998, Art. no. 3228, doi: 10.1063/1.363264.

[7] V. Potin, P. Ruterana, G. Nouet, and R. Pond, "Mosaic growth of GaN on (0001) sapphire: A high-resolution electron microscopy and crystallographic study of threading dislocations from low-angle to high-angle grain boundaries," *Phys. Rev. B*, vol. 61, no. 8, Feb. 2000, Art. no. 5587, doi: 10.1103/PhysRevB.61.5587.

[8] F. Shahedipour-Sandvik et al., "Origin of ring defects in high in content green InGaN/GaN MQW: An Ultrasonic force microscopy study," *Mater. Res. Soc. Internet J. Nitride Semicond. Res.*, vol. 10, no. 1, Oct. 2005, Art. no. e4, doi: 10.1557/S1092578300000557.

[9] X. H. Wu et al., "Structural origin of V-defects and correlation with localized excitonic centers in InGaN/GaN multiple quantum wells," *Appl. Phys. Lett.*, vol. 72, no. 6, Jun. 1998, Art. no. 692, doi: 10.1063/1.120844.

[10] H. K. Cho, J. Y. Lee, and G. M. Yang, "Formation mechanism of V defects in the InGaN/GaN multiple quantum wells grown on GaN layers with low threading dislocation density," *Appl. Phys. Lett.*, vol. 79, 2001, Art. no. 215, doi: 10.1063/1.1384906.

[11] Y. Chen et al., "Pit formation in GaInN quantum wells," *Appl. Phys. Lett.*, vol. 72, no. 6, Jun. 1998, Art. no. 710, doi: 10.1063/1.120853.

[12] C. J. Sun et al., "Quantum shift of band-edge stimulated emission in InGaN–GaN multiple quantum well light-emitting diodes," *Appl. Phys. Lett.*, vol. 70, no. 22, Jun. 1998, Art. no. 2978, doi: 10.1063/1.118762.

[13] I. H. Kim, H. S. Park, Y. J. Park, and T. Kim, "Formation of V-shaped pits in InGaN/GaN multiquantum wells and bulk InGaN films," *Appl. Phys. Lett.*, vol. 73, no. 12, Sep. 1998, Art. no. 1634, doi: 10.1063/1.122229.

[14] F. C. P. Massabuau et al., "Carrier localization in the vicinity of dislocations in InGaN," *J. Appl. Phys.*, vol. 121, no. 1, Jan. 2017, Art. no. 013104, doi: 10.1063/1.4973278.

[15] J.-Y. Chung et al., "Light-emitting V-pits: An alternative approach toward luminescent indium-rich InGaN quantum dots," *ACS Photon.*, vol. 8, pp. 2853–2860, 2021, doi: 10.1021/acsphotonics.1c01009.

[16] M. Dmukauskas et al., "Correlation between growth interruption and indium segregation in InGaN MQWs," *J. Lumin.*, vol. 221, May 2020, Art. no. 117103, doi: 10.1016/J.JLUMIN.2020.117103.

[17] J. Zhang et al., "Study on carrier transportation in InGaN based green LEDs with V-pits structure in the active region," *Opt. Mater. (Amst.)*, vol. 86, pp. 46–50, Dec. 2018, doi: 10.1016/J.OPTMAT.2018.09.017.

[18] S. L. Selvaraj, A. Watanabe, and T. Egawa, "Influence of deep-pits on the device characteristics of metal-organic chemical vapor deposition grown AlGaN/GaN high-electron mobility transistors on silicon substrate," *Appl. Phys. Lett.*, vol. 98, no. 25, Jun. 2011, Art. no. 252105, doi: 10.1063/1.3602919.

[19] F. Liang et al., "Performance deterioration of GaN-based laser diode by V-pits in the upper waveguide layer," *Nanophotonics*, vol. 9, no. 3, pp. 667–674, Mar. 2020, doi: 10.1515/NANOPH-2019-0449/MACHINEREADABLECITATION/RIS.

[20] S. Zhou and X. Liu, "Effect of V-pits embedded InGaN/GaN superlattices on optical and electrical properties of GaN-based green light-emitting diodes (Phys. Status Solidi A 5/2017)," *Physica Status Solidi*, vol. 214, no. 5, May 2017, Art. no. 1770125, doi: 10.1002/PSSA.201770130.

[21] S. W. Chen, C. J. Chang, and T. C. Lu, "Effect of strains and V-shaped pit structures on the performance of GaN-based light-emitting diodes," *Crystals*, vol. 10, no. 4, Apr. 2020, Art. no. 311, doi: 10.3390/CRYST10040311.

[22] A. Hospodková et al., "InGaN/GaN structures: Effect of the quantum well number on the cathodoluminescent properties," *Physica Status Solidi*, vol. 255, no. 5, May 2018, Art. no. 1700464, doi: 10.1002/PSSB.201700464.

[23] T. Hubáček et al., "Advancement toward ultra-thick and bright InGaN/GaN structures with a high number of QWs," *CrystEngComm*, vol. 21, no. 2, pp. 356–362, Jan. 2019, doi: 10.1039/C8CE01830H.

[24] W. Lee et al., "Cross sectional CL study of the growth and annihilation of pit type defects in HVPE grown (0001) thick GaN," *J. Cryst. Growth*, vol. 351, no. 1, pp. 83–87, Jul. 2012, doi: 10.1016/J.JCRYSGRO.2012.04.016.

[25] Z. Gao et al., "Influence of lateral growth on the surface pit formation of GaN heteroepitaxial film grown by MOCVD," *Mater. Sci.*, vol. 22, no. 2, pp. 223–227, Jun. 2016, doi: 10.5755/J01.MS.22.2.12931.

[26] X. Huang et al., "Energy band engineering of InGaN/GaN multi-quantum-well solar cells via AlGaN electron- and hole-blocking layers," *Appl. Phys. Lett.*, vol. 113, no. 4, Jul. 2018, Art. no. 043501, doi: 10.1063/1.5028530.

[27] A. Caria et al., "Excitation intensity and temperature-dependent performance of InGaN/GaN multiple quantum wells photodetectors," *Electronics*, vol. 9, no. 11, Nov. 2020, Art. no. 1840, doi: 10.3390/ELECTRONICS9111840.

[28] A. Caria et al., "GaN-based solar cells degradation kinetics investigated at high temperature under high-intensity 405nm optical stress," *SPIE. Conf. Proc.*, vol. 12001, pp. 44–51, Mar. 2022, doi: 10.1117/12.2608680.

[29] M. Nicoletto et al., "Role of p-GaN layer thickness in the degradation of InGaN-GaN MQW solar cells under 405 nm laser excitation," *Microelectronics Rel.*, vol. 138, Nov. 2022, Art. no. 114727, doi: 10.1016/J.MICROREL.2022.114727.

[30] M. Mandurrino et al., "Physics-based modeling and experimental implications of trap-assisted tunneling in InGaN/GaN light-emitting diodes," *Physica Status Solidi Appl. Mater. Sci.*, vol. 212, no. 5, pp. 947–953, May 2015, doi: 10.1002/PSSA.201431743.

[31] M. Auf Der Maur et al., "Trap-assisted tunneling in InGaN/GaN single-quantum-well light-emitting diodes," *Appl. Phys. Lett.*, vol. 105, no. 13, 2014, Art. no. 133504, doi: 10.1063/1.4896970.

[32] N. Roccato et al., "Modeling the electrical characteristics of InGaN/GaN LED structures based on experimentally-measured defect characteristics," *J. Phys. D Appl. Phys.*, vol. 54, no. 42, Aug. 2021, Art. no. 425105, doi: 10.1088/1361-6463/AC16FD.

[33] M. Musolino et al., "A physical model for the reverse leakage current in (In,Ga)N/GaN light-emitting diodes based on nanowires," *J. Appl. Phys.*, vol. 119, no. 4, 2016, Art. no. 044502, doi: 10.1063/1.4940949.

[34] A. M. Yong, C. B. Soh, X. H. Zhang, S. Y. Chow, and S. J. Chua, "Investigation of V-defects formation in InGaN/GaN multiple quantum well grown on sapphire," *Thin Solid Films*, vol. 515, no. 10, pp. 4496–4500, Mar. 2007, doi: 10.1016/J.TSF.2006.07.181.

[35] J. Stránská Matějová et al., "V-pits formation in InGaN/GaN: Influence of threading dislocations and indium content," *J. Phys. D Appl. Phys.*, vol. 55, no. 25, Mar. 2022, Art. no. 255101, doi: 10.1088/1361-6463/AC5C1A.

[36] S. Kitamura, K. Hiramatsu, and N. Sawaki, "Fabrication of Gan hexagonal pyramids on dot-patterned Gan/Sapphire substrates via selective metalorganic vapor phase epitaxy," *Jpn. J. Appl. Phys.*, vol. 34, no. 9, pp. L1184–L1186, Sep. 1995, doi: 10.1143/JJAP.34.L1184/XML.

[37] C. M. Tsai et al., "High efficiency and improved ESD characteristics of GaN-based LEDs with naturally textured surface grown by MOCVD," *IEEE Photon. Technol. Lett.*, vol. 18, no. 11, pp. 1213–1215, Jun. 2006, doi: 10.1109/LPT.2006.875063.

[38] Synopsys and Inc, "SentaurusTM Mesh User Guide," 2015. [Online]. Available: http://www.synopsys.com/Company/Pages/Trademarks.aspx

[39] Synopsys and Inc, "SentaurusTM device user guide," 2015. [Online]. Available: http://www.synopsys.com/Company/Pages/Trademarks.aspx

[40] L. Silvestri, K. Dunn, S. Prawer, and F. Ladouceur, "Hybrid functional study of Si and O donors in wurtzite AlN," *Appl. Phys. Lett.*, vol. 99, no. 12, Sep. 2011, Art. no. 122109, doi: 10.1063/1.3641861.

[41] Y. Nakano and T. Jimbo, "Electrical properties of acceptor levels in Mg-doped GaN," *Physica Status Solidi*, no. 1, pp. 438–442, Dec. 2002, doi: 10.1002/PSSC.200390082.

[42] C. Z. Zhao, T. Wei, L. Y. Chen, S. S. Wang, and J. Wang, "The activation energy for Mg acceptor in AlxGa1-xN alloys in the whole composition range," *Superlattices Microstructures*, vol. 109, pp. 758–762, Sep. 2017, doi: 10.1016/J.SPMI.2017.06.006.

[43] W. Götz et al., "Activation energies of Si donors in GaN," *ApPhL*, vol. 68, no. 22, pp. 3144–3146, 1996, doi: 10.1063/1.115805.

[44] N. S. Averkiev et al., "Two channels of non-radiative recombination in InGaN/GaN LEDs," *Physica B*, vol. 404, no. 23/24, pp. 4896–4898, Dec. 2009, doi: 10.1016/J.PHYSB.2009.08.252.

[45] S. D. Nehate, A. Prakash, P. D. Mani, and K. B. Sundaram, "Work function extraction of indium tin oxide films from MOSFET devices," *ECS J. Solid State Sci. Technol.*, vol. 7, no. 3, pp. P87–P90, Feb. 2018, doi: 10.1149/2.0081803JSS/XML.

[46] Y. J. Lin, "Comment on 'contact mechanisms and design principles for alloyed ohmic contacts to n-GaN," *J. Appl. Phys.*, vol. 100, no. 7, Oct. 2006, Art. no. 073707, doi: 10.1063/1.2353254.

[47] Q. Wu et al., "Effects of the number of wells on the performance of green InGaN/GaN LEDs with V-shape pits grown on Si substrates," *Superlattices Microstructures*, vol. 114, pp. 89–96, Feb. 2018, doi: 10.1016/J.SPMI.2017.12.012.

[48] Z. Quan, L. Wang, C. Zheng, J. Liu, and F. Jiang, "Roles of V-shaped pits on the improvement of quantum efficiency in InGaN/GaN multiple quantum well light-emitting diodes," *J. Appl. Phys.*, vol. 116, no. 18, Nov. 2014, Art. no. 183107, doi: 10.1063/1.4901828.

[49] T. L. Song, S. J. Chua, E. A. Fitzgerald, P. Chen, and S. Tripathy, "Characterization of graded InGaN/GaN epilayers grown on sapphire," *J. Vac. Sci. Technol. A, Vac., Surfaces, Films*, vol. 22, no. 2, pp. 287–292, Mar. 2004, doi: 10.1116/1.1644114.

[50] T. L. Song, S.-J. Chua, and E. A. Fitzgerald, "Graded InGaN buffers for strain relaxation in GaN/InGaN epliayers grown on sapphire," 2002. Accessed: Dec. 6, 2022. [Online]. Available: https://dspace.mit.edu/handle/1721.1/3975

Open Access funding provided by 'Università degli Studi di Padova' within the CRUI CARE Agreement